Effect of Post-translational Modifications and Mutations on Amyloid-β fibrils Dynamics at N-terminus

Liliya Vugmeyster,^{1,*} Dan F. Au,¹ Dmitry Ostrovsky,² Brian Kierl,¹ Riqiang Fu,³ Zhi-wen Hu,⁴ Wei Qiang⁴

*To whom correspondence should be addressed: Liliya Vugmeyster, 1201 Laurimer Street, Denver CO 80204, USA email: LILIYA.VUGMEYSTER@UCDENVER.EDU

Running title: Variant Flexibility of N-terminal of AB

Keywords: amyloid-β, post-translational modifications, deuterium NMR, protein dynamics, solid state NMR, disordered protein domain, protein misfolding

Abstract

We investigate the variability in the dynamics of the disordered N-terminal domain of amyloid-β fibrils $(A\beta)$, comprising residues 1–16 of $A\beta_{1.40}$, due to post-translational modifications (PTMs) and mutations in the β-bend regions known to modulate aggregation properties. Using ²H static solid-state NMR approaches, we compare the dynamics in the wild-type AB fibrils in the 3-fold symmetric polymorph with the fibrils from three PTM sequences: isoaspartate-D7, the phosphorylation of S8 (pS8), and an N-terminal truncation Δ E3. Additional comparisons are made with the mutants in the β -bend region (residues 21–23) corresponding to the familial Osaka E22A deletion and D23N Iowa mutation. We also include the aggregates induced by Zn²⁺ ions. The dynamics are probed at the F4 and G9 positions. The main motional model involves two free states undergoing diffusion and conformational exchanges with the bound state in which the diffusion is quenched due to transient interactions involving fibril core and other intra-strand contacts. The fraction of the bound state increases in a sigmoidal fashion with a decrease in temperature. There is clear variability in the dynamics: the pS8 variant is the most rigid at the G9 site in line with structural studies, the $\Delta E3$ fibrils are more flexible at the G9 site in line with the morphological fragmentation pattern, the Zn-induced aggregates are the most mobile, and the two β-bend mutants have the strongest changes at the F4 site toward higher rigidity. Overall, the changes underlie the potential role of conformational ensembles in setting the stage for aggregation-prone states.

Statement of Significance: In this work we demonstrate variations of motions in the disordered region of amyloid-beta fibrils due to modifications induced either by naturally occurring mutations or post-translational modifications. The results indicate clear variability in the flexibility of the disordered domain and its potential role in modulating aggregation-prone states.

¹ Department of Chemistry, University of Colorado Denver, Denver CO USA 80204

² Department of Mathematics, University of Colorado Denver, Denver CO USA 80204

³ National High Field Magnetic Laboratory, Tallahassee, FL USA 32310

⁴Department of Chemistry, Binghamton University, Binghamton, New York USA 13902

Introduction

Amyloid- β peptide (A β) aggregation remains to be viewed as one of the causative factors in Alzheimer's disease (AD) as a part of the amyloid hypothesis. (1-4) It is believed that A β accumulation is a trigger that initiates a pathological cascade implicating tau protein, synuclein, and other aggregation-prone proteins.(2, 3) The structural polymorphism of amyloid fibrils is a challenging and potentially pathologically important factor in the molecular basis of AD.(5-9) This polymorphism occurs at multiple levels,(10) leading to many possible fibrillar structures from the same Aß protein as well as the existence of multiple molecular variants of AB including 1-39, 1-40, and 1-42 and the variants of these with post-translational modifications (PTMs) and mutations. The majority of PTMs occur in the flexible N-terminal region of the fibrils, encompassing residues 1–16, and are thought to trigger or accelerate the fibrillation of wild-type Aβ peptides.(2, 11, 12) However, the pathological roles of modified AB in AD have not been determined in detail. It has been suggested that PTMs may be responsible for sporadic cases of AD, which encompass 90% of all patients.(2, 11) On the contrary, many familial-type mutations that cause the early onset of the disease occur around the \(\beta\)-bend region of A\(\beta\), comprising residues 21–23, and are associated with altered folds, higher aggregation propensities, and higher toxicities.(13-17) Metal ions are also known to alter aggregation propensities. In particular, animal models show that Zn^{2+} coordination can play a crucial role in the formation of plagues in vivo.(18-20) At concentrations of the order of what is found at synapses, Zn²⁺ specifically binds to Aβ and promotes aggregation.(21, 22) The resulting multitude of the structural ensembles, combined with the differential seeding abilities of the variants, can have profound implications on the existence of the most aggressive forms as well as on the effectiveness of the initiation of the pathological cascades of the aggregation of other related proteins.

One of the ways in which to characterize the ensembles is probing the flexibility of the structures.(10) We compare the dynamics in wild-type $A\beta_{1-40}$ in one of its more toxic polymorphs possessing 3-fold symmetry(23) with two PTMs occurring around the "hot-spot" 6–8 region(10) of the N-terminal domain, an N-terminal truncation PTM, and two mutants corresponding to familial mutations in the β -bend 21–23 region of the fibrils. In particular, we investigate PTMs corresponding to the phosphorylation of Ser-8(pS8), aspartate to iso-aspartate at position D7 (isoD7), the truncation variant corresponds to the cleavage of the peptide bond between positions 2 and 3 (Δ E3), as well as the Osaka E22 Δ deletion mutant and D23N Iowa mutant of the β -bend region. Additionally, we include in the comparison the results for the aggregates formed by wild-type $A\beta_{1-40}$ in the presence of Zn^{2+} ions (Zn). Below, we present the relevant backgrounds of these variants.

The E22 Δ A β_{1-40} deletion mutation has been found to be more neurotoxic in rat primary neuron cultures than wild-type A β .(24) Previous works have characterized the 2-fold symmetric structure displaying the in-register parallel β -sheet as well as determined the mass per length (MPL) measurements.(25) The cross-section of the fibril can be approximated by a rectangle defined by an additional intermolecular salt bridge between the Glu3 and Lys28 side chains, which seems to be absent in wild-type models. A unique feature of the fibrils is that they form extremely fast and show very low levels of thioflavin T fluorescence with no lag phase.(26) The E22 Δ variant has also been shown to efficiently cross-seed the wild-type protein.(27)

One of the essential features of the D23N $A\beta_{1-40}$ Iowa mutant is its ability to form an antiparallel β -sheet structure.(28-31) The polymorph of D23N with the antiparallel β -sheet structures are relatively short and curved fibril-like intermediates. They are metastable and eventually convert into mature D23N fibrils, which have parallel β -sheet structures similar to wild-type $A\beta$ fibrils.(29, 31, 32) The structural unit is a monomer in this case. The hydrophobic core is somewhat less compact than the wild-type.

The pS8 modification has recently been shown to have a strong cross-seeding ability for wild-type A β , (33)and its structure as well as the dynamics of the core region have been determined by solid-state nuclear

magnetic resonance (NMR).(34) S8 phosphorylation has been shown to play an important role in late-onset sporadic AD(35, 36), especially associated with the symptomatic pathology.(37) It may also display increased nucleation-dependent fibrillation and enhance Aβ-mediated toxicity.(11, 38) The pS8 fibrils show the 2-fold symmetric structure with the in-register parallel β -sheet and striated-ribbon morphology similar to the 2-fold wt-A β ₁₋₄₀ when grown under similar conditions.(34) However, the fibrils are about 2.5 nm wider. The highest structural distinction were observed in the N-terminal region. In particular, the variant showed strong intra-strand interactions between the N-terminus and rest of the amyloid core. Additionally, the hydrophobic core packing was more pronounced than the wild-type and the side chain dynamics more restricted in the core.

The isoD7 PTM has been found to increase aggregation propensities and zinc-dependent oligomerization (12, 39, 40). In parenchymal plaque core preparations, iso-aspartate is the predominant form at position #7.(12, 41) *In vitro*, this type of isomerization has also been suggested to lead to an enhanced propensity to form β -sheets as well as enhanced insolubility and resistance to enzymatic degradation.(12, 42-44) The intriguing study by Fonseca et al. suggested that the amount of isoD7 in plaques can serve as an indication of plaque age.(45) Fukuda et al.(43) demonstrated that $A\beta_{1-42}$ does not form fibrils in the presence of isoD7 modification. In this study, we work with the isoD7 sequence cross-seeded with wild-type $A\beta_{1-40}$ to promote fibrillation. For this variant, as the structure is not available, we supplement an NMR investigation with the MPL characterization of these fibrils based on tilted beam transmission electron microscopy (TEM) measurements.(46)

It has been suggested that the shortening of the N-terminus may lead to higher aggregation propensity.(12, 47, 48) One example is the 3-Glutamate truncation ($\Delta E3$) seen in plaques originating from late AD cases as well as in mouse-based models of AD.(49) This truncation also serves as a starting point for the generation of the pyroglutamate-3 aggressive modification. The enhanced aggregation propensity in these PTMs may be at least partially attributed to the reduced polarity and enhanced hydrophobicity from the deletion of charged residues at N-termini.(48) Morphologies and fibrillation kinetics have been found to be similar between the $\Delta E3$ and pyroglutamate-3 variants and in general faster than the fibrillation of other N-terminal PTM sub-types.(50) Scheidt et al.(51) utilized solid-state NMR to compare the structures of the pyroglutamate-3 and the wild-type fibrils and concluded that the cores are rather similar structurally, although the N-terminus shows alteration in the dynamics based on the backbone order parameters probed at the C_{α} sites. This study did not tackle the $\Delta E3$ precursor itself, however.

This work focuses on investigating the dynamics of the flexible N-terminal region of the fibrils, which is known to be important for the regulation of aggregation control.(52-58) The general flexibility of non-core regions in A β has been demonstrated by multiple techniques such as NMR,(59-67) electron paramagnetic resonance,(68) hydrogen-deuterium exchange,(69-71) X-ray crystallography,(72) and fluorescence spectroscopy.(73) Fawzi et al. utilized solution NMR saturation transfer approaches to probe the binding of monomeric A β to the surface of protofibrils.(74, 75) The site-specific characterization of dynamics in aggregated forms remains challenging due to the difficulties of obtaining site-specific resolution. Many structures (including wild-type structures)(61) have been unable to include the first nine residues of A β due to the mobility of these sites.

We recently investigated the dynamics of the N-terminal subdomain in wild-type fibrils by probing the motions of hydrophobic side chains using ²H solid-state NMR methods combined with residue-specific deuteration.(76, 77) The N-terminal domain participates in a number of motional modes, including the overall diffusion-like motion at two different timescales and the conformational exchange process that could be attributed to the transient interactions of the N-terminal domain with the structured hydrophobic core. At 37°C, we observed a progressive freezing of the dynamics along the sequence, characterized by an increased fraction of the bound state and reduction in the overall diffusive motion of the domain.

The goal of this work is the detailed comparison of the N-terminal domain dynamics among the variants described above. The dynamics are probed at the F4 site belonging to the more flexible N-terminal end and the G9 site at which the dynamics are significantly reduced in wild-type fibrils (Figure 1).(77) The differential dynamics in all these variants underscores conformational sampling, which likely contributes to differentiating the aggregation propensities and cross-seeding aggressiveness.

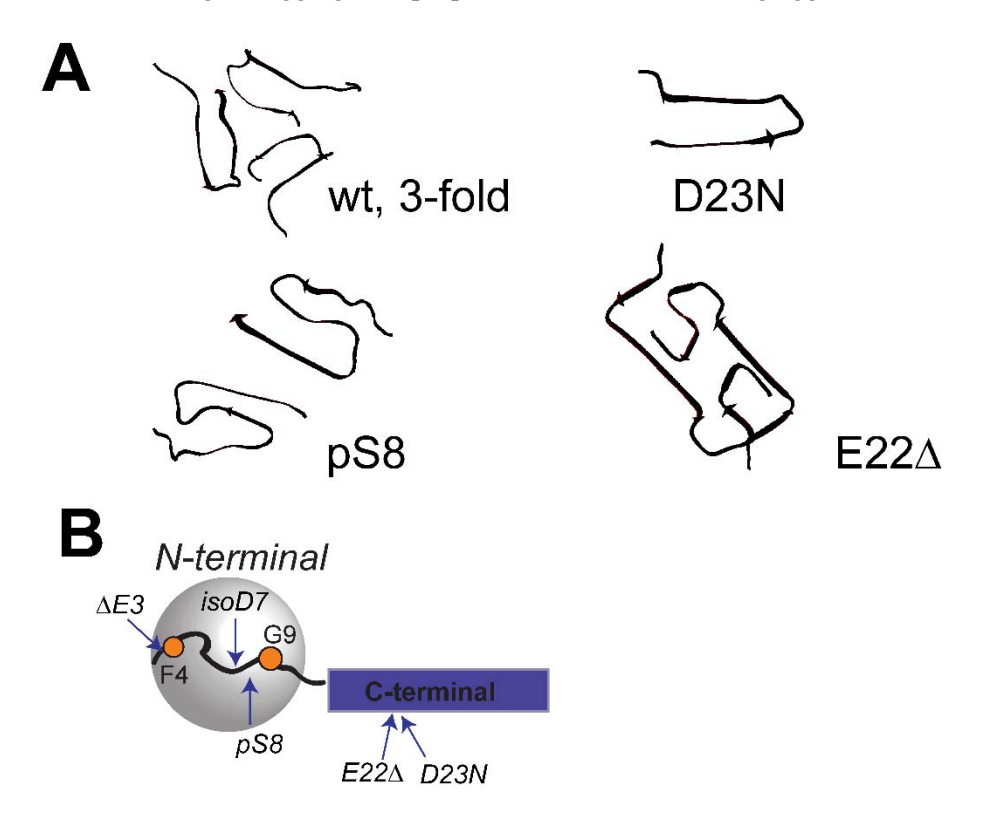


Figure 1. A) Quaternary structure for the variants studied in this work for which the structural coordinates are available: wild-type 3-fold symmetric structure, 2LMP. pdb ID;(23) pS8 post-translational modification with the 2-fold symmetric structure, 6OC9.pdb;(34) monomeric structure of the Iowa D23N mutant with the antiparallel β-sheet structure, 2LNQ.pdb;(31) Osaka E22 Δ mutation with the rectangular cross-section, 2MVX.pdb.(25) B) Schematic representation of the domains of A β_{1-40} , with the flexible N-terminal domain (residues 1–16, gray sphere) and C-terminal domain spanning the core (blue rectangle). Modified sequences investigated in this work are marked with arrows: Δ E3, isoD7, and pS8 located in the N-terminal domain and E22 Δ and D23N located in the β -bend region of the C-terminal domain. The sites of the deuterium isotope labels on the side chains of F4 and G9 are shown as orange dots. The labeling patterns are ring-D₅ for F4 and α CD₂ for G9.

Materials and Methods

Peptide synthesis: The $A\beta_{1-40}$ peptides were prepared by using solid-state peptide synthesis (performed by Thermofisher Scientific Co, Rockford, IL). Fluorenylmethyloxycarbonyl (FMOC)-Phenylalanine-ring- d_5 and FMOC-Glycine- C_{α} - d_2 , were purchased from Cambridge Isotopes Laboratories (Andover, MA). Further details are listed in the Supplementary Material File S1. The resulting peptides had isotopic labels in only one chosen residue, either F4 or G9.

Fibrils preparation: The pS8 and Δ E3: fibrils were grown following the generation seeding protocol developed previously.(34, 78). IsoD7 cross-seeded with wild-type A β_{1-40} : the seeds consisted of the wild-type A β_{1-40} fibrils in the 3-fold symmetric polymorph and were used in 1:10 molar ratio of the wild-type

 $A\beta_{1-40}$ seeds to the isoD7. E22 Δ fibrils were prepared at 0.3 mg/mL concentration and TEM images were taken immediately upon dissolving in the buffer, at 2-3 hours and at 24-30 hours after dissolution. Details of these procedures are listed in the Supplementary Material File S1. Preparation of the D23N fibrils with anti-parallel β -sheet structure utilized a two-step seeding/filtration cycle that takes advantage of the differences in fibril formation rate between the parallel and anti-parallel structures. (31) Zn^{2+} -induced aggregates were prepared as described in the earlier work(77) . After pelleting and lyophilizing of the fibrils, the hydrated state with a water content of 200% by weight was achieved by pipetting deuterium-depleted H_2O . The samples were packed in 5 mm NMR tubes (cut to 21 mm length) using Teflon tape to center the sample volume in the coil of the NMR probe.

NMR spectroscopy: Line shape experiments were performed with a quadrupole echo pulse sequence. (79) The $R_{1\rho}$ experiments were performed at 9.4 T and 37°C using the methodology described in previous work (80) with the pulse sequence of Figure S1. The relaxation decay curves M(t) corresponding to the integration of the central narrow component (up to the half-height intensity) were fitted to a single exponential function with an offset: $M(t) = Ae^{-t/T_{1\rho}} + B$. ²H QCPMG time-domain measurements (Figure S1) (81) were performed at 14.1 T field strength and 37°C. Integrated echo intensities were fitted to a single exponential function with no offset. Further details are listed in the Supplementary Material File S1.

Fitting of freezing curves: The data for p_{bound} were fitted to the function:

$$p_{bound} = a + \frac{b - a}{1 + \exp\left(\frac{T - T_m}{\sigma}\right)} \tag{1}$$

in which $T_{\rm m}$ is the midpoint of the freezing curve, σ is the characteristic width of the transition region, and a and b are the higher and lower temperature baselines, respectively.

Results

Morphological patterns

The fibrils of the $A\beta_{1-40}$ variants exhibited different morphological patterns characterized by the negatively stained TEM technique (Figure 2 and additional images in Figure S2), consistent with the findings in the literature and our previous work.(26, 31, 33, 34, 82-84) The twisted 3-fold symmetric morphology of the wild-type fibrils (Figure 2 and previous analysis of the wild-type fibrils(77, 84)) contrasts with the straighter and thicker fibril filaments for the pS8 fibrils, relatively short straight fibrils for the Δ E3, curvy and short D23N fibrils, long and curvy E22 Δ fibrils, and amorphous Zn²⁺-induced aggregates. Two additional observations are worth noting: for the E22 Δ mutant, the fibrils reached the final morphologies in 2–3 hours (Figure S3), in line with previous studies.(26) In addition, the fragmentation pattern observed for the Δ E3 morphology was similar to that of the pyroglutamate-3 fibrils (Figure S4 and Wulff et al.(50)).

For the isoD7 variant cross-seeded with wild-type 3-fold A β , the morphology was largely conserved. To further quantify the dimensions of the fibrils resulting from cross-seeding isoD7 with the wild-type fibrils in the 3-fold polymorph, we performed a detailed MPL analysis. Specifically, we employed tilted beam TEM (dark-field imaging), which is effective for the statistical characterization of the MPL of fibrils.(46, 85, 86) Both the 2-fold and the 3-fold polymorphs of native A β_{1-40} (61, 82) have previously been analyzed using this technique.(46) The results (Figure S5) indicated that the predominant polymorph is closer in its MPL to the 3-fold wild-type variant (around 90% of the fibrils), with a small proportion of the 2-fold characteristics. Further studies are needed to assess whether this trend is general; in this study, we suffice with characterization of our bulk samples used in the NMR analysis.

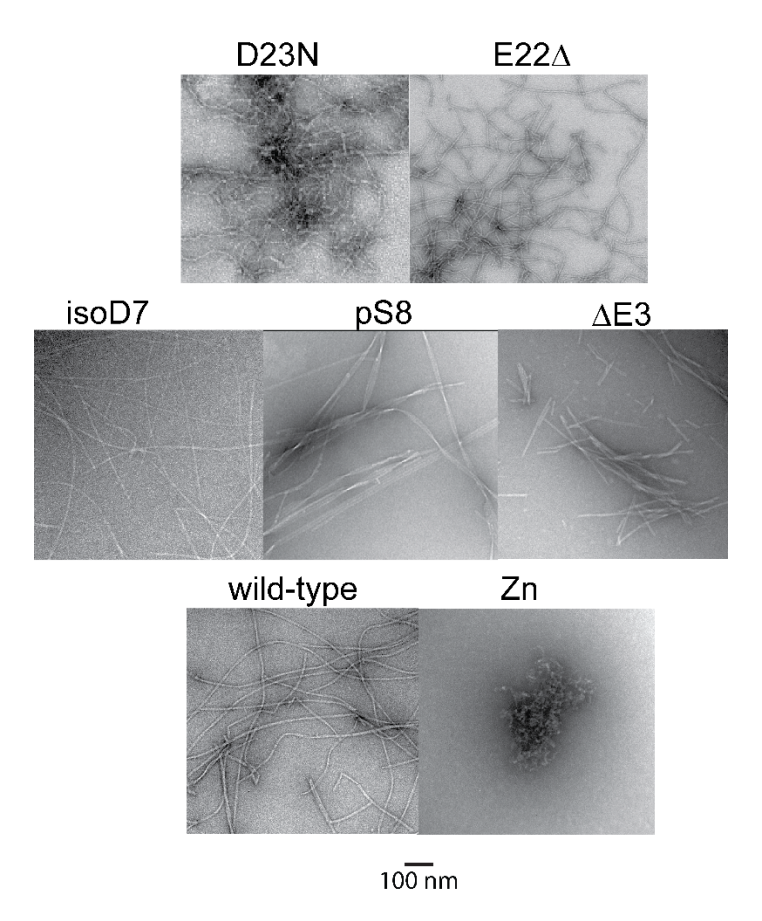


Figure 2. Typical examples of the negatively stained transmission electron microscopy images of fibrils from different variants investigated in this study.

Overview of the general model of N-terminal flexibility and approaches

For each of the fibril types, two samples were prepared for the NMR analysis: one containing a deuterium label at the F4 position, ring-D₅, and another at the G9 position, ${}^{\alpha}\text{CD}_2$.

We recently demonstrated that ${}^{2}H$ rotating frame relaxation ($R_{1\rho}$) and Quadrupolar Carr-Purcell-Meiboom-Gill (QCPMG) transverse relaxation measurements provide a comprehensive view of conformational exchange processes.(76) Although both these techniques are sensitive to motions on the biologically relevant μ s-ms timescales, they provide complementary information on the motional modes.

In this section, we review the motional models employed to fit all the experimental data. The motional model in Figure 3A, which was developed based on the data for the wild-type protein, (76) includes three states of the N-terminal domain: two "free" mobile states in which the N-terminal undergoes large-angle diffusion motion and one bound state in which the diffusive motion in quenched, most likely due to transient interactions with the structured fibril core or transient intra-strand interactions with N-terminal domains of neighboring chains (Figure 3D). In the free state restricted rotational diffusion is very pronounced and we assume an isotropic scenario for the local motional axis (i.e., phenyl axis for the case of F4 and two-fold rotation axis for the case of G9 CD₂ group). This is not to be confused with global isotropic diffusion of macromolecules in solution – the fibrils are only 200% by weight hydrated with most of the water contributing to the hydration shell.

The diffusion coefficients in the two free states differ by about two orders of magnitude difference between the two states, $D_1 \gg D_2$. Each of the free states undergoes a conformational exchange process with the bound

state, with the rate constants of $k_{\text{ex},1}$ and $k_{\text{ex},2}$, respectively. For the G9 sites, in two of the variants, this model cannot fit the data. For the Zn-induced aggregates, no conformational exchange that involves the bound state is detected; rather, the exchange between the two free states is invoked (Figure 3B). For the D23N fibrils, only a single free state has the "slow" diffusion coefficient of D_2 (Figure 3C).

The model of Figure 3A has been developed as the simplest scheme based on the extensive data on the dynamics of the wild-type A β fibrils. It does not incorporate any structural constraints other than a physical intuition on what would be in general consistent with the known structures of the fibrils. In particular, we do not assume any specific structural constraints for the transient interactions between the free and bound states. Additionally, the approximation of the isotropic diffusion and two different conformational states of the N-terminal domain is possibly reflecting a much more complex situation with anisotropic motions and an ensemble of multiple states, in analogy to the existence of tethered states found for monomers on the surface of protofibrils.(74, 75) Within the available dynamics data, invoking these more complex models would be a clear overfitting of the data. For consistency, we keep the model the same for all of the A β variants, unless a clear need arises to introduce modifications based on the data. We also note that the line shape data alone could be modeled based on assumption of two static non-exchanging fractions with rigid and motionally narrowed tensors. However, our previous analysis of the longitudinal relaxation data for the wild-type fibrils in conjunction with $R_{1\rho}$ measurements precludes the use of such model.

We show that depending on the quadrupolar interaction magnitude and timescale of motion, QCPMG and R_{1p} experiments are sensitive to different conformational exchange processes. For the F4 residues, the effective quadrupolar tensor is narrow, with an effective quadrupolar coupling constant of $C_q = 36.6$ kHz after averaging over the rotameric motions of the side chain. On the contrary, for the G9, the effective C_q is 77.6 kHz after averaging over the two-site jumps of the CD₂ group. As a result, the QCPMG experiment primarily probes the conformational exchange between the free state with a fast diffusion state and the bound state (D_1 , rate constant $k_{\text{ex},1}$) for the F4 sites and the free slow diffusion state and the bound state (D_2 , rate constant $k_{\text{ex},2}$) for the G9 sites. The situation is reversed for the R_{1p} experiment: it is most sensitive to the conformational exchanges between the fast diffusion free state and bound state for the G9 sites as well as between the slow diffusion state and bound state for the F4 sites. The relative populations of the two free states are obtained by fitting the data to the full model in Figure 3A.

The fraction of the bound state p_{bound} was taken from the line shape analysis. p_{bound} as a function of temperature follows a sigmoidal curve indicative of a relatively abrupt freezing of the diffusion motions. This approach is not based on any assumptions regarding possible structural changes induced by lowering the temperature, i.e. p_{bound} only reports on the cumulative increase of intra and inter- molecular interactions that lead to line broadening. The midpoint freezing temperature T_{m} (see Eq. (1)) increases along the N-terminal domain chain for the wild-type protein. While, for the residues close to the N-terminal end (A2 to H6 sites), it appears to be dictated by the freezing of the hydration layer (~267 K), T_{m} increases along the sequence and is at 284 K for the G9.(77) p_{bound} at the physiological temperature increases from 8–10% in the A2–H6 region, to 35% for the G9, to 85% at the V12 site. Thus, to probe the dynamics of all the variants, we selected labels at the F4 and G9 locations to capture the details of the dynamics in the more flexible N-terminal domain region and the region in which the dynamics can be more restricted due to more pronounced interactions with the core. R_{1p} measurements are conducted for four values of spin-locking field strength and QCPMG measurements for at least seven values of inter-pulse spacing. Between these relaxation data and p_{bound} determination from the line shape analysis, there are enough data points to determine all model parameters.

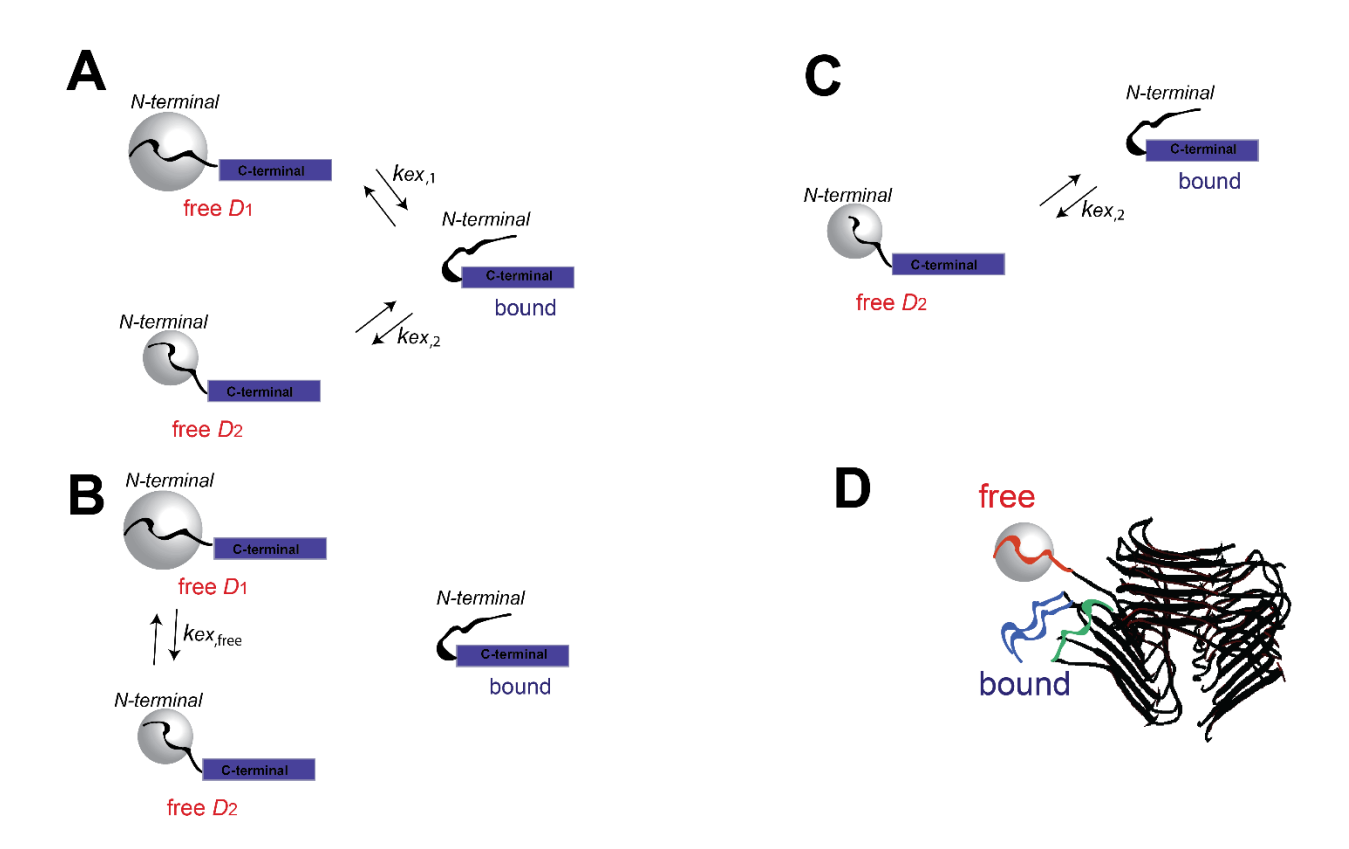


Figure 3. Modeling schemes for the motions of the disordered N-terminal domain (residues 1-16) of the Aβ₁₋₄₀ fibrils. A). Three-state motional model in which the N-terminal domain (curved line) transiently interacts with the structured C-terminal domain (blue rectangle).(76) In the two free states, the N-terminal domain is assumed to undergo isotropic diffusion with the diffusion coefficients D_1 and D_2 , $D_1 \gg D_2$, represented by the gray spheres, while in the bound state, the interactions quench this mode. The timescales of the interactions are given by the two chemical exchange rate constants, $k_{\text{ex},1}$ and $k_{\text{ex},2}$, respectively. Most sites were fit with this full model. B) Modification of model A for which there is no conformational exchange between the free and bound states on the experimental timescales, but instead exchange between the two free states with the rate constant $k_{\text{ex},\text{free}}$. Applicable to the Zn²⁺ aggregates at the G9 site. C) Sub-model of A) in which there is no fast free diffusion state, only a slow free diffusion state. Applicable to the D23N sample at the G9 site. D). Schematic representation of free (orange wiggly line) and bound (blue and green wiggly lines) states of N-terminal subdomain with the 3-fold wild-type fibrils structure. The 3-fold symmetric fibril core is taken from 2LMP. pdb file(23) and is shown as black ribbon diagram. Bound state can arise either due to transient interactions with the core (green lines) or transient tight stacking with the neighboring N-terminal strand (blue lines). In the free state (orange wiggly line) the domain can undergo relatively large scale fluctuations, which are not possible in any of the bound states.

²H NMR line shape analysis yields the fraction of the bound state

The 2 H line shape is a simple one-dimensional experiment performed with a quadrupolar echo pulse sequence(79) that provides a wealth of information on the dynamics close to the timescale of the effective quadrupolar coupling constant. At the physiological temperature, for all variants, the line shapes significantly narrow and they approach solution-like line shapes (Figure 4), indicating the presence of large-scale motions on the relevant timescale. With a decrease in temperature, the wide component of the powder pattern becomes apparent. The narrow component is attributed to the free states undergoing motions approximated by the isotropic diffusion. The wide component is attributed to the "bound" state, which lacks diffusive motions, presumably due to interactions with the rigid fibril core. The p_{bound} for the F4 residue is quantified by decomposing the line shape into its Lorenzian and non-Lorenzian components,(77) the latter of which is attributed to the of the bound state (see the examples in Figure S6). Similar to the treatment of

the wild-type fibrils, (77) the analysis for the G9 sites is somewhat more complex, with p_{bound} spanning the subset of the non-Lorenzian contribution corresponding to the rigid pattern. Interestingly, for the pS8 G9 site at high temperatures, it appears that the bound state has a different chemical shift than the free states (Figure S6). The p_{bound} for all residues (Figure 5) follows the characteristic sigmoidal behavior observed for the wild-type protein, and this can be fitted to Eq. (1), which yields the midpoint of the freezing curves T_{m} and width of the transition σ , summarized in Figure 6 along with the results for the fraction of the bound state p_{bound} at the physiological temperature.

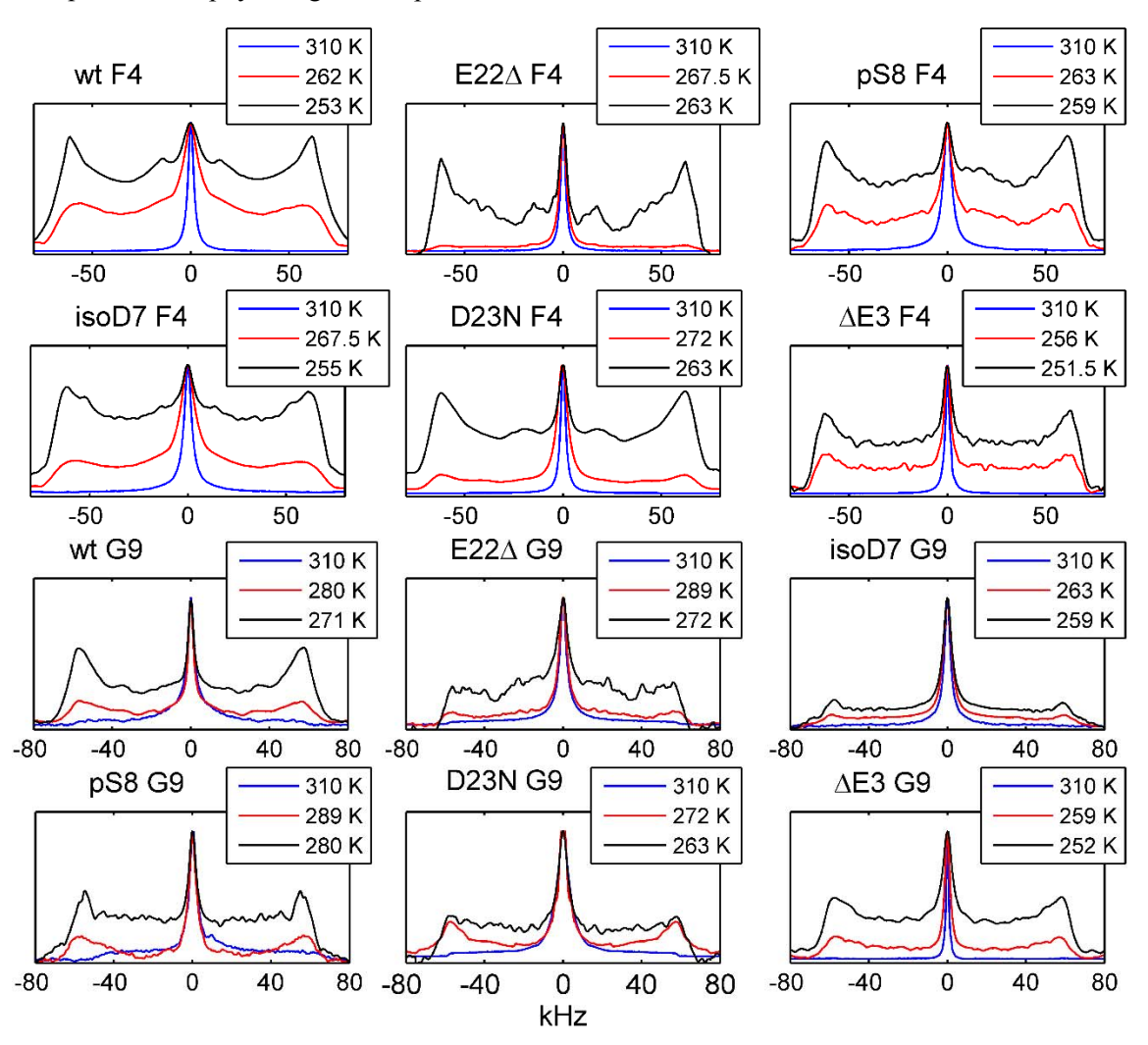


Figure 4. Representative 2H static solid-state NMR line shape data in the hydrated fibril samples of $A\beta_{1-40}$ at 310 K and two intermediate temperatures. The isotope labeling patterns are F4-ring-D₅ and G9-C $_{\alpha}$ D₂. The data for the wild-type fibrils are taken from an earlier work.(77)

The higher value of $T_{\rm m}$ signifies that the onset of the freezing of the diffusion motions starts at a higher temperature upon sample cooling. Most variants display a gap in $T_{\rm m}$ value between the F4 and G9 sites of 5–20°. For the Δ E3 fibrils, the value of $T_{\rm m}$ is 262–263 K for both sites; for D23N, it is 273 K for both sites (Figure 6). The largest gap of 20° is for the pS8 fibrils. Interestingly, the width of the transition is maintained at a higher value for the G9 sites (average value of 7°) in comparison with F4 for all samples (with an average value of 2.1°). The higher values of σ may reflect stronger interactions with the core with a distribution of distances between the probed site and contacts within the core, leading to a wider transition. Further, the value of $p_{\rm bound}$ at 37°C is consistently higher (0.14–0.42) than that of F4 (0.06–0.18) for all

samples (Figure 6). There is clear variability in the fitted values of $T_{\rm m}$ between the different A β variants. For example, the pS8 variant has the highest $T_{\rm m}$ and highest $p_{\rm bound}$ for the G9 site. This result is in line with a recent structural study(34) pointing to a more structured N-terminal domain. The $T_{\rm m}$ values at the G9 sites are much lower for the Δ E3, isoD7, and D23N variants. It is also of note that the line shapes at the physiological temperature are wider for the D23N variant for both sites, pointing to the possibility of a slower conformational exchange between the free and bound states, as detailed later in the text.

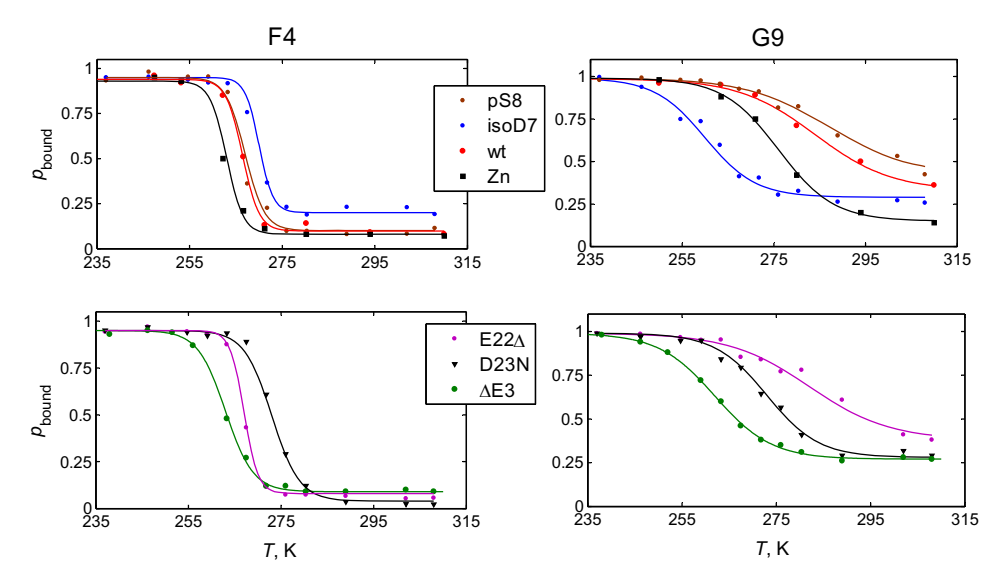


Figure 5. p_{bound} derived from the line shape decomposition as a function of temperature. The solid lines represent the fits according to Eq. (1). The data for the wild-type fibrils and Zn²⁺-induced aggregates are taken from an earlier work.(77)

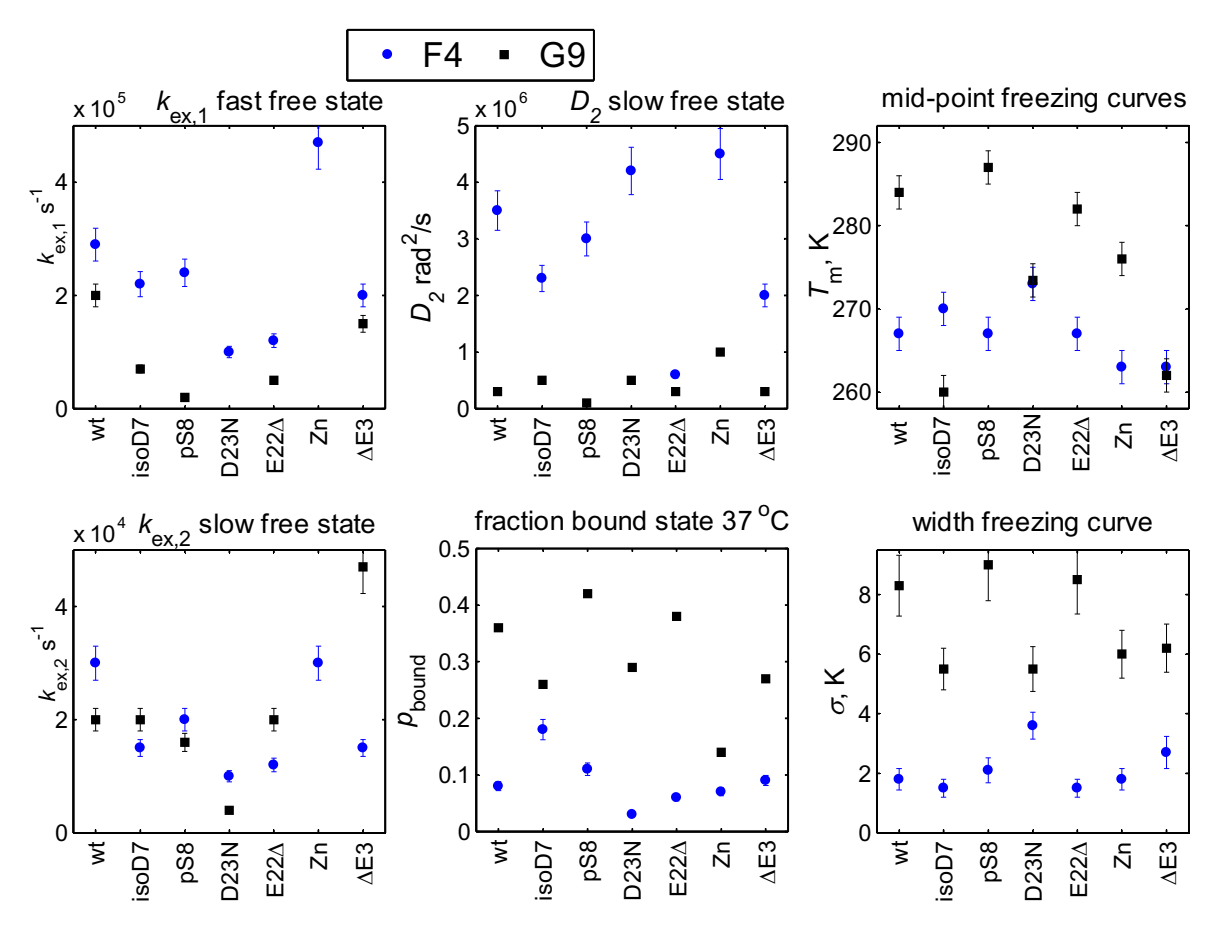


Figure 6. Summary of the model parameters according to the full model in Figure 3A and the fits of the freezing curves. The rate constants are $k_{\text{ex,1}}$, $k_{\text{ex,2}}$, D_2 , p_{bound} , T_{m} , and σ . D_1 is in the fast limit and is at least 0.7–1 10^8 rad²/s. The relative percentages of the populations of the free to slow diffusion state are as follows: 70/30 for the F4 sites of wt and Zn; 60/40 for the F4 sites of Δ E3, isoD7, E22 Δ , and pS8; 20/80 for the F4 site of D23N; and 5/95 to 10/90 for all the G9 sites except for D23N for which it is zero (see the model in Figure 3C) and Zn for which it is around 50/50. The Zn G9 site is fitted with the model in Figure 3B with $k_{\text{ex,free}} = 250 \text{ s}^{-1}$. Error bars smaller than the sizes of the symbols are not shown.

²H QCPMG and R_{1p} relaxation measurements provide the conformational exchange rate constants and diffusion coefficients of the free states

To probe the timescales of the conformational exchange and obtain the most accurate values of the diffusion coefficients, it is necessary to perform more complicated measurements known to be sensitive to conformational exchange processes at the μs to ms timescale, such as the QCPMG and $R_{1\rho}$ measurements(87-90) briefly described in the "Overview of the model" section above. Our earlier work describes the technical details of these measurements and the fitting procedure based on the models using the full Liouvillian treatment of relaxation.(76, 80) Here, we focus on the results, which were obtained at the physiological temperature.

The 2 H QCPMG experiment under static conditions (see Supplementary Material File S1 and Figure S1A) is performed by measuring the transverse relaxation rates as a function of the spacing of the refocusing pulses, τ_{QCPMG} , using a time domain approach. Motions on the timescale of τ_{QCPMG} interfere with the refocusing of magnetization, and the extent of this interference depends on the inter-pulse spacing. Interestingly, the dispersion profiles are the reverse of those traditionally seen in solution CPMG experiments, likely due to the anisotropic nature of the quadrupolar interactions.(76, 89) For the 2 H R_{1p}

experiment under static conditions (Figure S1B),(80) refocusing is accomplished by the variable spin-locking field, ω_{SL} .

Figure 7 summarizes the experimental relaxation times and Figure S7 provides examples of the raw data. The variability between the samples is immediately apparent for both experiments. For the D23N sample at the G9 site, the R_{1p} rate was too fast to be measured accurately.

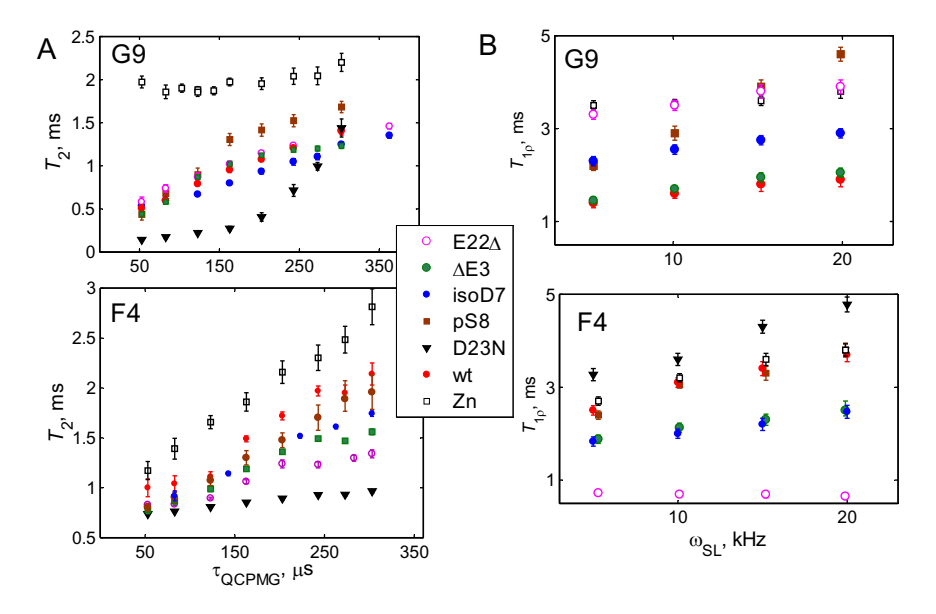


Figure 7. A) Experimental transverse relaxation time T_2 as a function of τ_{QCPMG} in the hydrated fibril samples of Aβ₁₋₄₀ derived from the time domain QCPMG experiment, collected at 37°C and 14.1 T. B) Experimental ²H $T_{1\rho} = 1/R_{1\rho}$ relaxation times at 37°C and 9.4 T. Error bars smaller than the sizes of the symbols are not shown.

As noted, defining the magnitude of the quadrupolar interaction is important, as this governs which timescales can be obtained from the two experiments. For the G9 site, we used the tensor with a quadrupolar coupling constant C_q of 77.6 kHz and the asymmetry parameter $\eta = 1$, as previously determined.(77) The tensor corresponds to the effective value averaged over fast two-site jumps of the CD2 group, which followed from the longitudinal relaxation results for the wild-type samples. For F4, we started with the tensor corresponding to the averaging over the fast two-site π -flips of the ring, consistent with the longitudinal relaxation data. However, this tensor leads to rate constants for the F4 site in the wild-type fibrils that are orders of magnitude smaller than those found for the A2 and H6 sites, inferring the presence of additional motions that affect the QCPMG and R_{1p} rates and lead to a lower effective C_q value. We thus invoke a two-site rotameric exchange involving the χ_1 and χ_2 dihedral angles. Specifically, we assume the existence of the rotamers found by Drobny and co-workers for one of the phenylalanine residues of the mineral recognition domain of the biomineralization protein salivary statherin adsorbed onto its native hydroxyapatite:(91) conformer one has $\chi_1=186.2^{\circ}$ and $\chi_2=88.6^{\circ}$, while conformer two has $\chi_1=274.7^{\circ}$ and χ_2 =54.8°. The ratio of the populations is taken as 1:1. In the fast limit, this leads to an effective tensor of C_q =36.6 kHz and η of 0.94. This tensor provides diffusion coefficients and rate constants for the wild-type fibrils perfectly in line with those of the A2 and H6 residues, allowing us to conclude that the additional rotameric motion is a good approximation of the additional mode affecting the relaxation rates.

All the F4 sites followed the model in Figure 3A. For the G9 sites, there are two exceptions: as noted, D23N in the G9 site had a very fast R_{1p} decay that could not be measured. Based on the analysis of the model for the wild-type fibrils,(76) this signifies the almost complete absence of the fast diffusion state, and thus this site is fitted with a single free state (Figure 3C). For the G9 site in the Zn²⁺-induced aggregates, the model in Figure 3A cannot be used; however, the model in which the exchange is dominated by the two free states

(Figure 3B) is adequate. The QCPMG- T_2 data are qualitatively different in this variant, with higher T_2 values and, most importantly, negligible dispersion.

The variations in the experimental rates are reflected in the fitted values of D_2 , $k_{\text{ex},1}$, and $k_{\text{ex},2}$. Figure 6 summarizes the main parameters of the model and Figure S8 provide examples of the fits of the experimental relaxation rates. The diffusion constant for the fast diffusion state D_1 is in the fast limit, and thus we can only state its lower limit, which falls to 0.7–1 10⁸ rad²/s. The conformational exchange rate constant $k_{\text{ex},1}$ for the wild-type for this state is $3 \cdot 10^5 \text{ s}^{-1}$ for the A2, F4, and H6 sites and $2 \cdot 10^5 \text{ s}^{-1}$ for the G9 sites. The variants' range for $k_{\text{ex},1}$ is $1.2-4.7 \cdot 10^5 \text{ s}^{-1}$ for F4 and $0.7-5 \cdot 10^5 \text{ s}^{-1}$ for G9. The slow diffusion state values of D_2 are $3.5 \cdot 10^6$ rad²/s and $3.0 \cdot 10^5$ rad²/s for the wild-type F4 and G9 sites, respectively. The range of the variants is $0.6-4.5 \cdot 10^6 \text{ rad}^2/\text{s}$ for the F4 sites and $3-10 \cdot 10^5 \text{ rad}^2/\text{s}$ for the G9 sites. The conformational exchange rate constant $k_{\text{ex},2}$ is $3\cdot10^4$ s⁻¹ for the A2, F4, and H6 sites in the wild-type protein and $2\cdot10^4$ s⁻¹ for G9. The ranges of the variants are $1-3 \cdot 10^4 \, \text{s}^{-1}$ and $0.4-4.7 \cdot 10^4 \, \text{s}^{-1}$ for the F4 and G9 sites, respectively. For the G9 site of the Zn²⁺-induced aggregates, the exchange rate constant between the two free states (see model in Figure 3B) is 250 s⁻¹. The relative percentage of the fast to slow diffusion free states at the F4 site is the largest for the wt and Zn variants (70/30%) and decreases somewhat (60/40%) for the other variants except for D23N in which it is drastically reduced to 20/80%. The fast state "freezes" to 5-10% for all samples for the G9 site and to zero for the D23N site, whereas it remains at around 50/50% for the Zn G9 site.

Discussion and Concluding Remarks

The N-terminal domain remains flexible for all the considered variants and the models of motions are in general similar; however, the extent of this flexibility varies among sequences. The three-state model involving two free states undergoing isotropic diffusion and one bound state (Figure 3A) is applicable to most sites, with the exceptions noted for the D23N fibrils and Zn²⁺-induced aggregates at the G9 position. Relatively significant variations exist in the parameters of the motions such as the conformational exchange rate constants and diffusion coefficients of the slower diffusion free states. All the protein sequences also display sigmoidal behavior in the fraction of the bound state upon lowering the temperature as well as variability in the mid-points of the freezing curves.

The patterns of mobility modulations in all the variants are complex; however, certain essential features emerge from the analysis, as summarized in Table 1. The pS8 fibrils, which were determined to have accelerated seeded fibrillation kinetics and enhanced toxicities as well as a more rigid core and a more structured N-terminus than the wild-type protein using structural techniques, (34) appear to have the most rigid dynamics. Due to a larger extent of intra-strand contacts in the structure between the N-terminal domain and the core for the fibrils in pS8, one might also expect a larger value of σ for the G9 site, but this is not the case based on the experimental data. The Δ E3 fibrils tend toward higher mobility at the G9 site in line with the morphological fragmentation. A morphologically similar fragmentation is observed for the fibrils in the presence of the cyclization to the pyroglutamate-3(50) (see also Figure S4), suggesting that similar changes in the N-terminal dynamics are likely to be present for this PTM as well. There is no clear pattern for the isoD7 fibrils cross-seeded with wild-type Aβ, which has a mixture of changed dynamical features. The most drastic change is seen for the value of $T_{\rm m}$ at the G9 site, which is about 15-20° lower than for the most of the other types of fibrils. This underscores the need for high resolution structural data for the isoD7 fibrils. Based on the structural, kinetics, morphological, and N-terminal dynamics information available for the ΔE3, pyroglutamate-3, pS8, and isoD7 variants,(11, 33, 34, 43, 50, 51, 92) all these PTMs are likely to have different cross-seeding abilities, which remains to be elucidated in follow-up work.

For the β -bend region mutation, the most interesting observation is that the modulation of the dynamics compared with the wild-type protein appears to occur closer to the N-terminal end. Indeed, many of the changes toward the restriction of the dynamics can be seen at the F4 site rather than the G9 site. The salt

bridge involving E3 may play a role in this restriction for the case of E22 Δ . However, no such salt bridge was seen for the antiparallel β -sheet structure of the D23N fibrils and, in general, this mutations leads to a less compact fibrils core,(31) and thus the restriction of the dynamics cannot be explained solely by the structural features in this case. Moreover, the p_{bound} value at the F4 site of the D23N fibrils is considerably lower than those of the other residues (Figure 6). However, this does not indicate an enhancement of the dynamics compared with the other fibrils, as the line shapes are significantly wider due to the slow exchange dynamics. The Zn²⁺-induced aggregates have a clear pattern of overall enhanced mobility in the N-terminus with more pronounced changes at the G9 sites, which is in line with the expectation that the hydrophobic core is less defined in these types of amorphous aggregates, leading to weaker interactions with the N-terminal domain.

Overall, these changes indicate that the dynamics information is complementary to the structural data and often it is not straightforward to predict in which direction the dynamics will change upon structural modifications. The results imply that the presence of intricate conformational ensembles can play an important role in the onset of aggregation-prone states and in the differentiation of cross-seeding aggressiveness, thus contributing to the overall polymorphism paradigm. Similar conformational exchange processes may be present in the toxic oligomeric forms, as conformational exchange has been detected for the monomer on the surface of the protofibrils by solution NMR measurements.(74, 75) Our study underlines the need to consider both structural and dynamics information when characterizing the disordered regions of the various toxic variants of $A\beta$ and other aggregation-prone proteins along AD pathways.

Table 1. Summary of the most essential changes (with at least three standard deviations) compared with the wild-type. The change toward the more rigid value is in blue; the change toward more enhanced dynamics is in red.

Variant	Parameters significantly different	Overall conclusion
	from the wild-type fibrils	
pS8	$k_{\text{ex},1}$ -G9, D_2 -G9, T_{m} -G9	Most rigid of all fibrils at G9, in line
		with structural information
ΔΕ3	$T_{\rm m}$ -G9, $k_{\rm ex,2}$ -G9	Tendency toward higher mobility at G9,
		in line with morphology fragmentation
isoD7	p_{bound} -F4, $k_{\text{ex},1}$ -G9, T_{m} -G9	Mixture of higher and lower mobility
cross-seeded with wt		features, no clear patterns
D23N	$T_{\rm m}$ -F4; $k_{\rm ex,1}$ -F4, σ -F4, $k_{\rm ex,2}$ -F4, $T_{\rm m}$ -	Most differences of all fibrils at F4
	G9, no fast diffusion state for G9,	(more rigid)
	$k_{\rm ex,2}$ -G9	
Ε22Δ	<i>D</i> ₂ -F4, <i>k</i> _{ex,2} -F4, <i>k</i> _{ex,1} -F4, <i>k</i> _{ex,1} -G9	Significant differences at F4 toward
		rigidity
Zn ²⁺ aggregates	$k_{\text{ex},1}$ -F4, no bound state exchange for	Overall enhanced mobility but more so
	G9, $T_{\rm m}$ -G9, $p_{\rm bound}$ -G9, D_2 -G9	at G9 site

Author Contributions. L.V. conceived and coordinated the project, designed and performed NMR experiments, and wrote the paper with input from all the authors. D.F.A. prepared some of the fibrils samples and performed TEM analysis with contribution from B.K. and performed some of NMR measurements. Z.H. prepared pS8 fibrils. W.Q. prepared D23N fibrils and performed MPL TEM measurements and analysis. D.O. performed modeling with input from L.V. R.F. contributed to the development of NMR methodology and data collection. All authors discussed the results.

Acknowledgments

This work was supported by a National Institutes of Health Grant 1R15-GM111681 and NSF grant 1726947. Some of the experiments were performed at the National High Magnetic Field Laboratory, which is supported by NSF Cooperative Agreement NSF/DMR-1644779, the State of Florida, and the U.S. Department of Energy.

Supplementary Material

File S1. Details of Experimental and Modeling Procedures. Figure S1. NMR QCPMG and $R_{1\rho}$ experiments pulse sequence. Figure S2. Additional examples of negatively stained TEM images Figure S3. TEM images of the E22 Δ fibrils time series. Figure S4. TEM image of pyroglutamate-E3 fibrils. Figure S5. MPL data for isoD7 fibrils. Figure S6. Line shape decomposition examples. Figure S7. Examples of QCPMG and $R_{1\rho}$ magnetization decay curves. Figure S8. Representative fits for QCPMG and $R_{1\rho}$ rates.

Supporting Citations

References (93-102) appear in the Supporting Material.

References

- 1. Hardy, J., and D. J. Selkoe. 2002. The Amyloid Hypothesis of Alzheimer's Disease: Progress and Problems on the Road to Therapeutics. Science. 297:353-356.
- 2. Barykin, E. P., V. A. Mitkevich, S. A. Kozin, and A. A. Makarov. 2017. Amyloid β Modification: A Key to the Sporadic Alzheimer's Disease? Front. Genet. 8:58-58.
- 3. Musiek, E. S., and D. M. Holtzman. 2015. Three dimensions of the amyloid hypothesis: time, space and 'wingmen'. Nat. Neurosci. 18:800-806.
- 4. Hardy, J., and G. Higgins. 1992. Alzheimer's disease: the amyloid cascade hypothesis. Science. 256:184-185.
- 5. Paravastu, A. K., R. D. Leapman, W. M. Yau, and R. Tycko. 2008. Molecular structural basis for polymorphism in Alzheimer's beta-amyloid fibrils. Proc. Natl. Aca. Sci. U.S.A. 105:18349-18354.
- 6. Tycko, R. 2015. Amyloid polymorphism: structural basis and neurobiological relevance. Neuron. 86:632-645.
- 7. Qiang, W., W. M. Yau, J. X. Lu, J. Collinge, and R. Tycko. 2017. Structural variation in amyloid-beta fibrils from Alzheimer's disease clinical subtypes. Nature. 541:217-221.
- 8. Lu, J. X., W. Qiang, W. M. Yau, C. D. Schwieters, S. C. Meredith, and R. Tycko. 2013. Molecular structure of beta-amyloid fibrils in Alzheimer's disease brain tissue. Cell. 154:1257-1268.
- 9. Rasmussen, J., J. Mahler, N. Beschorner, S. A. Kaeser, L. M. Hasler, F. Baumann, S. Nystrom, E. Portelius, K. Blennow, T. Lashley, N. C. Fox, D. Sepulveda-Falla, M. Glatzel, A. L. Oblak, B. Ghetti, K. P. R. Nilsson, P. Hammarstrom, M. Staufenbiel, L. C. Walker, and M. Jucker. 2017. Amyloid polymorphisms constitute distinct clouds of conformational variants in different etiological subtypes of Alzheimer's disease. Proc. Natl. Acad. Sci. U S A. 114:13018-13023.
- 10. Hubin, E., N. A. J. van Nuland, K. Broersen, and K. Pauwels. 2014. Transient dynamics of A beta contribute to toxicity in Alzheimer's disease. Cell. Mol. Life Sci. 71:3507-3521.
- 11. Roher, A. E., T. A. Kokjohn, S. G. Clarke, M. R. Sierks, C. L. Maarouf, G. E. Serrano, M. S. Sabbagh, and T. G. Beach. 2017. APP/Aβ structural diversity and Alzheimer's disease pathogenesis. Neurochem. Int. 110:1-13.
- 12. Kummer, M. P., and M. T. Heneka. 2014. Truncated and modified amyloid-beta species. Alzheim. Reser. Ther. 6.
- 13. Gessel, M. M., S. Bernstein, M. Kemper, D. B. Teplow, and M. T. Bowers. 2012. Familial Alzheimer's disease mutations differentially alter amyloid β-protein oligomerization. ACS Chem. Neurosci. 3:909-918.

- 14. Hatami, A., S. Monjazeb, S. Milton, and C. G. Glabe. 2017. Familial Alzheimer's Disease Mutations within the Amyloid Precursor Protein Alter the Aggregation and Conformation of the Amyloid-beta Peptide. J. Biol. Chem. 292:3172-3185.
- 15. Jang, H., F. T. Arce, S. Ramachandran, B. L. Kagan, R. Lal, and R. Nussinov. 2013. Familial Alzheimer's disease Osaka mutant (DeltaE22) beta-barrels suggest an explanation for the different Abeta1-40/42 preferred conformational states observed by experiment. J. Phys. Chem. B. 117:11518-11529.
- 16. Gessel, M. M., S. Bernstein, M. Kemper, D. B. Teplow, and M. T. Bowers. 2012. Familial Alzheimer's disease mutations differentially alter amyloid beta-protein oligomerization. ACS Chem. Neurosci. 3:909-918.
- 17. Baumketner, A., S. L. Bernstein, T. Wyttenbach, N. D. Lazo, D. B. Teplow, M. T. Bowers, and J.-E. Shea. 2006. Structure of the 21-30 fragment of amyloid beta-protein. Prot. Sci. 15:1239-1247.
- 18. Bush, A. I. 2013. The Metal Theory of Alzheimer's Disease. J. Alzheim. Dis. 33:S277-S281.
- 19. Hamley, I. W. 2012. The Amyloid Beta Peptide: A Chemist's Perspective. Role in Alzheimer's and Fibrillization. Chem. Rev. 112:5147-5192.
- 20. Ayton, S., P. Lei, and A. I. Bush. 2015. Biometals and Their Therapeutic Implications in Alzheimer's Disease. Neurotherapeutics. 12:109-120.
- 21. Suh, S. W., K. B. Jensen, M. S. Jensen, D. S. Silva, P. J. Kesslak, G. Danscher, and C. J. Frederickson. 2000. Histochemically-reactive zinc in amyloid plaques, angiopathy, and degenerating neurons of Alzheimer's diseased brains. Brain. Reser. 852:274-278.
- 22. Lovell, M. A., J. D. Robertson, W. J. Teesdale, J. L. Campbell, and W. R. Markesbery. 1998. Copper, iron and zinc in Alzheimer's disease senile plaques. J. Neurol. Sci. 158:47-52.
- 23. Paravastu, A. K., I. Qahwash, R. D. Leapman, S. C. Meredith, and R. Tycko. 2009. Seeded growth of beta-amyloid fibrils from Alzheimer's brain-derived fibrils produces a distinct fibril structure. Proc. Natl. Aca. Sci. U.S.A. 106:7443-7448.
- 24. Ovchinnikova, O. Y., V. H. Finder, I. Vodopivec, R. M. Nitsch, and R. Glockshuber. 2011. The Osaka FAD mutation E22Delta leads to the formation of a previously unknown type of amyloid beta fibrils and modulates Abeta neurotoxicity. J. Mol. Biol. 408:780-791.
- 25. Schutz, A. K., T. Vagt, M. Huber, O. Y. Ovchinnikova, R. Cadalbert, J. Wall, P. Guntert, A. Bockmann, R. Glockshuber, and B. H. Meier. 2015. Atomic-resolution three-dimensional structure of amyloid beta fibrils bearing the Osaka mutation. Angew. Chem. Int. Ed. 54:331-335.
- 26. Cloe, A. L., J. P. Orgel, J. R. Sachleben, R. Tycko, and S. C. Meredith. 2011. The Japanese mutant Abeta (DeltaE22-Abeta(1-39)) forms fibrils instantaneously, with low-thioflavin T fluorescence: seeding of wild-type Abeta(1-40) into atypical fibrils by DeltaE22-Abeta(1-39). Biochemistry. 50:2026-2039.
- 27. Tomiyama, T., T. Nagata, H. Shimada, R. Teraoka, A. Fukushima, H. Kanemitsu, H. Takuma, R. Kuwano, M. Imagawa, S. Ataka, Y. Wada, E. Yoshioka, T. Nishizaki, Y. Watanabe, and H. Mori. 2008. A new amyloid beta variant favoring oligomerization in Alzheimer's-type dementia. Ann. Neurol. 63:377-387.
- 28. Grabowski, T. J., H. S. Cho, J. P. G. Vonsattel, G. W. Rebeck, and S. M. Greenberg. 2001. Novel amyloid precursor protein mutation in an Iowa family with dementia and severe cerebral amyloid angiopathy. Ann. Neurol. 49:697-705.
- 29. Qiang, W., W. M. Yau, and R. Tycko. 2011. Structural Evolution of Iowa Mutant beta-Amyloid Fibrils from Polymorphic to Homogeneous States under Repeated Seeded Growth. J. Am. Chem. Soc. 133:4018-4029.
- 30. Tycko, R., K. L. Sciarretta, J. Orgel, and S. C. Meredith. 2009. Evidence for Novel beta-Sheet Structures in Iowa Mutant beta-Amyloid Fibrils. Biochemistry. 48:6072-6084.
- 31. Qiang, W., W. M. Yau, Y. Q. Luo, M. P. Mattson, and R. Tycko. 2012. Antiparallel beta-sheet architecture in Iowa-mutant beta-amyloid fibrils. Proc. Natl. Acad. Sci. U.S.A. 109:4443-4448.

- 32. Sgourakis, N. G., W. M. Yau, and W. Qiang. 2015. Modeling an In-Register, Parallel "Iowa" A beta Fibril Structure Using Solid-State NMR Data from Labeled Samples with Rosetta. Structure. 23:216-227.
- 33. Hu, Z.-W., M.-R. Ma, Y.-X. Chen, Y.-F. Zhao, W. Qiang, and Y.-M. Li. 2017. Phosphorylation at Ser8 as an Intrinsic Regulatory Switch to Regulate the Morphologies and Structures of Alzheimer's 40-residue β-Amyloid (Aβ40) Fibrils. J. Biol. Chem. 292:2611-2623.
- 34. Hu, Z. W., L. Vugmeyster, D. F. Au, D. Ostrovsky, Y. Sun, and W. Qiang. 2019. The Molecular Structure of a "Seeding-Prone" N-terminal Phosphorylated b-Amyloid Fibril. Proc. Natl. Acad. Sci. U.S.A. 116: 11253-11258
- 35. Kumar, S., and J. Walter. 2011. Phosphorylation of amyloid beta (Abeta) peptides a trigger for formation of toxic aggregates in Alzheimer's disease. Aging. 3:803-812.
- 36. Kumar, S., O. Wirths, S. Theil, J. Gerth, T. A. Bayer, and J. Walter. 2013. Early intraneuronal accumulation and increased aggregation of phosphorylated Abeta in a mouse model of Alzheimer's disease. Acta neuropathologica. 125:699-709.
- 37. Rijal Upadhaya, A., I. Kosterin, S. Kumar, C. A. von Arnim, H. Yamaguchi, M. Fandrich, J. Walter, and D. R. Thal. 2014. Biochemical stages of amyloid-beta peptide aggregation and accumulation in the human brain and their association with symptomatic and pathologically preclinical Alzheimer's disease. Brain .137:887-903.
- 38. Kumar, S., N. Rezaei-Ghaleh, D. Terwel, D. R. Thal, M. Richard, M. Hoch, J. M. Mc Donald, U. Wullner, K. Glebov, M. T. Heneka, D. M. Walsh, M. Zweckstetter, and J. Walter. 2011. Extracellular phosphorylation of the amyloid beta-peptide promotes formation of toxic aggregates during the pathogenesis of Alzheimer's disease. EMBO J. 30:2255-2265.
- 39. Tsvetkov, P. O., I. A. Popov, E. N. Nikolaev, A. I. Archakov, A. A. Makarov, and S. A. Kozin. 2008. Isomerization of the Asp7 residue results in zinc-induced oligomerization of Alzheimer's disease amyloid beta(1-16) peptide. Chembiochem. 9:1564-1567.
- 40. Kozin, S. A., I. B. Cheglakov, A. A. Ovsepyan, G. B. Telegin, P. O. Tsvetkov, A. V. Lisitsa, and A. A. Makarov. 2013. Peripherally applied synthetic peptide isoAsp7-Abeta(1-42) triggers cerebral beta-amyloidosis. Neurotox. Res. 24:370-376.
- 41. Roher, A. E., J. D. Lowenson, S. Clarke, C. Wolkow, R. Wang, R. J. Cotter, I. M. Reardon, H. A. Zurcherneely, R. L. Heinrikson, M. J. Ball, and B. D. Greenberg. 1993. Structural alterations in the peptide backbone of beta-amyloid core protein may account for its deposition and stability in Alzheimer's disease. J. Biol. Chem. 268:3072-3083.
- 42. Kuo, Y. M., S. Webster, M. R. Emmerling, N. De Lima, and A. E. Roher. 1998. Irreversible dimerization/tetramerization and post-translational modifications inhibit proteolytic degradation of A beta peptides of Alzheimer's disease. Biochim. Biophys. Acta. 1406:291-298.
- 43. Fukuda, H., T. Shimizu, M. Nakajima, H. Mori, and T. Shirasawa. 1999. Synthesis, aggregation, and neurotoxicity of the Alzheimer's A beta 1-42 amyloid peptide and its isoaspartyl isomers. Bioorg. Med. Chem. Lett. 9:953-956.
- 44. Fabian, H., G. I. Szendrei, H. H. Mantsch, B. D. Greenberg, and L. ÖTvÖS. 1994. Synthetic post-translationally modified human Aβ peptide exhibits a markedly increased tendency to form β-pleated sheets in vitro. Europ. J. Biochem. 221:959-964.
- 45. Fonseca, M. I., E. Head, P. Velazquez, C. W. Cotman, and A. J. Tenner. 1999. The presence of isoaspartic acid in beta-amyloid plaques indicates plaque age. Exp. Neurol. 157:277-288.
- 46. Chen, B., K. R. Thurber, F. Shewmaker, R. B. Wickner, and R. Tycko. 2009. Measurement of amyloid fibril mass-per-length by tilted-beam transmission electron microscopy. Proc. Natl. Acad. Sci. U.S.A. 106:14339-14344.
- 47. Pike, C. J., M. J. Overman, and C. W. Cotman. 1995. Amino-terminal deletions enhance aggregation of beta-amyloid peptides in vitro. J. Biol. Chem. 270:23895-23898.
- 48. Dunys, J., A. Valverde, and F. Checler. 2018. Are N- and C-terminally truncated Abeta species key pathological triggers in Alzheimer's disease? J. Biol. Chem. 293:15419-15428.

- 49. Guntert, A., H. Dobeli, and B. Bohrmann. 2006. High sensitivity analysis of amyloid-beta peptide composition in amyloid deposits from human and PS2APP mouse brain. Neuroscience. 143:461-475.
- 50. Wulff, M., M. Baumann, A. Thummler, J. K. Yadav, L. Heinrich, U. Knupfer, D. Schlenzig, A. Schierhorn, J. U. Rahfeld, U. Horn, J. Balbach, H. U. Demuth, and M. Fandrich. 2016. Enhanced Fibril Fragmentation of N-Terminally Truncated and Pyroglutamyl-Modified Abeta Peptides. Angew. Chem. Int. Ed. 55:5081-5084.
- 51. Scheidt, H. A., J. Adler, M. Krueger, and D. Huster. 2016. Fibrils of Truncated Pyroglutamyl-Modified Aβ Peptide Exhibit a Similar Structure as Wildtype Mature Aβ Fibrils. Sci. Rep. 6:33531.
- 52. Mazzitelli, S., F. Filipello, M. Rasile, E. Lauranzano, C. Starvaggi-Cucuzza, M. Tamborini, D. Pozzi, I. Barajon, T. Giorgino, A. Natalello, and M. Matteoli. 2016. Amyloid-β 1–24 C-terminal truncated fragment promotes amyloid-β 1–42 aggregate formation in the healthy brain. Acta Neuropath. Commun. 4:110.
- 53. Brannstrom, K., A. Ohman, L. Nilsson, M. Pihl, L. Sandblad, and A. Olofsson. 2014. The Nterminal region of amyloid beta controls the aggregation rate and fibril stability at low pH through a gain of function mechanism. J. Am. Chem. Soc. 136:10956-10964.
- 54. Morris, C., S. Cupples, T. W. Kent, E. A. Elbassal, E. P. Wojcikiewicz, P. Yi, and D. Du. 2018. N-Terminal Charged Residues of Amyloid-beta Peptide Modulate Amyloidogenesis and Interaction with Lipid Membrane. Chemistry. 24:9494-9498.
- 55. Nussbaum, J. M., S. Schilling, H. Cynis, A. Silva, E. Swanson, T. Wangsanut, K. Tayler, B. Wiltgen, A. Hatami, R. Ronicke, K. Reymann, B. Hutter-Paier, A. Alexandru, W. Jagla, S. Graubner, C. G. Glabe, H. U. Demuth, and G. S. Bloom. 2012. Prion-like behaviour and taudependent cytotoxicity of pyroglutamylated amyloid-beta. Nature. 485:651-655.
- Kummer, M. P., M. Hermes, A. Delekarte, T. Hammerschmidt, S. Kumar, D. Terwel, J. Walter, H. C. Pape, S. Konig, S. Roeber, F. Jessen, T. Klockgether, M. Korte, and M. T. Heneka. 2011. Nitration of tyrosine 10 critically enhances amyloid beta aggregation and plaque formation. Neuron. 71:833-844.
- 57. Rezaei-Ghaleh, N., M. Amininasab, S. Kumar, J. Walter, and M. Zweckstetter. 2016. Phosphorylation modifies the molecular stability of beta-amyloid deposits. Nat Commun. 7:11359.
- 58. Xu, L., R. Nussinov, and B. Ma. 2016. Allosteric stabilization of the amyloid-β peptide hairpin by the fluctuating N-terminal. Chem. Commun. 52:1733-1736.
- 59. Scheidt, H. A., I. Morgado, S. Rothemund, and D. Huster. 2012. Dynamics of Amyloid beta Fibrils Revealed by Solid-state NMR. J. Biol. Chem. 287:2017-2021.
- 60. Luhrs, T., C. Ritter, M. Adrian, D. Riek-Loher, B. Bohrmann, H. Doeli, D. Schubert, and R. Riek. 2005. 3D structure of Alzheimer's amyloid-beta(1-42) fibrils. Proc. Natl. Acad. Sci. U.S.A. 102:17342-17347.
- 61. Petkova, A. T., W. M. Yau, and R. Tycko. 2006. Experimental constraints on quaternary structure in Alzheimer's beta-amyloid fibrils. Biochemistry. 45:498-512.
- 62. Bertini, I., L. Gonnelli, C. Luchinat, J. Mao, and A. Nesi. 2011. A New Structural Model of A beta(40) Fibrils. J. Am. Chem. Soc. 133:16013-16022.
- 63. Olofsson, A., A. E. Sauer-Eriksson, and A. Ohman. 2006. The solvent protection of Alzheimer amyloid-beta-(1-42) fibrils as determined by solution NMR spectroscopy. J. Biol. Chem. 281:477-483.
- 64. Whittemore, N. A., R. Mishra, I. Kheterpal, A. D. Williams, R. Wetzel, and E. H. Serpersu. 2005. Hydrogen-deuterium (H/D) exchange mapping of A ss(1-40) amyloid fibril secondary structure using nuclear magnetic resonance spectroscopy. Biochemistry. 44:4434-4441.
- 65. Prade, E., C. Barucker, R. Sarkar, G. Althoff-Ospelt, J. M. Lopez Del Amo, S. Hossain, Y. Zhong, G. Multhaup, and B. Reif. 2016. Sulindac Sulfide Induces the Formation of Large Oligomeric Aggregates of the Alzheimer's Disease Amyloid-beta Peptide Which Exhibit Reduced Neurotoxicity. Biochemistry. 55:1839-1849.

- 66. Linser, R., R. Sarkar, A. Krushelnitzky, A. Mainz, and B. Reif. 2014. Dynamics in the solid-state: perspectives for the investigation of amyloid aggregates, membrane proteins and soluble protein complexes. J. Biomol. NMR. 59:1-14.
- 67. Wang, T., H. Jo, W. F. DeGrado, and M. Hong. 2017. Water Distribution, Dynamics, and Interactions with Alzheimer's β-Amyloid Fibrils Investigated by Solid-State NMR. J. Am. Chem. Soc
- 68. Torok, M., S. Milton, R. Kayed, P. Wu, T. McIntire, C. G. Glabe, and R. Langen. 2002. Structural and dynamic features of Alzheimer's A beta peptide in amyloid fibrils studied by site-directed spin labeling. J. Biol. Chem. 277:40810-40815.
- 69. Kheterpal, I., S. Zhou, K. D. Cook, and R. Wetzel. 2000. A beta amyloid fibrils possess a core structure highly resistant to hydrogen exchange. Proc. Natl. Acad. Sci. U.S.A. 97:13597-13601.
- Wang, S. S. S., S. A. Tobler, T. A. Good, and E. J. Fernandez. 2003. Hydrogen exchange-mass spectrometry analysis of beta-Amyloid peptide structure. Biochemistry. 42:9507-9514.
- 71. Kheterpal, I., M. Chen, K. D. Cook, and R. Wetzel. 2006. Structural differences in A beta amyloid protofibrils and fibrils mapped by hydrogen exchange Mass spectrometry with on-line proteolytic fragmentation. J. Mol. Biol. 361:785-795.
- 72. Sawaya, M. R., S. Sambashivan, R. Nelson, M. I. Ivanova, S. A. Sievers, M. I. Apostol, M. J. Thompson, M. Balbirnie, J. J. W. Wiltzius, H. T. McFarlane, A. O. Madsen, C. Riekel, and D. Eisenberg. 2007. Atomic structures of amyloid cross-beta spines reveal varied steric zippers. Nature. 447:453-457.
- 73. Liu, H., C. Morris, R. Lantz, T. W. Kent, E. A. Elbassal, E. P. Wojcikiewicz, and D. Du. 2018. Residue-Specific Dynamics and Local Environmental Changes in Abeta40 Oligomer and Fibril Formation. Angew. Chem. Int. Ed. 57:8017-8021.
- 74. Fawzi, N. L., D. S. Libich, J. Ying, V. Tugarinov, and G. M. Clore. 2014. Characterizing Methyl-Bearing Side Chain Contacts and Dynamics Mediating Amyloid β Protofibril Interactions Using (13)C(methyl)-DEST and Lifetime Line Broadening. Angew .Chem. 53:10345-10349.
- 75. Fawzi, N. L., J. Ying, R. Ghirlando, D. A. Torchia, and G. M. Clore. 2011. Atomic-resolution dynamics on the surface of amyloid-beta protofibrils probed by solution NMR. Nature. 480:268-272.
- 76. Vugmeyster, L., D. F. Au, D. Ostrovsky, and R. Fu. 2019. Deuteron solid-state NMR relaxation measurements reveal two distinct conformational exchange processes in the disordered N-terminal domain of amyloid-b fibrils. ChemPhysChem. 20:1680.
- 77. Au, D. F., D. Ostrovsky, R. Fu, and L. Vugmeyster. 2019. Solid-state NMR reveals a comprehensive view of the dynamics of the flexible, disordered N-terminal domain of amyloid-β fibrils. J. Biol. Chem. 294:5840–5853.
- 78. Xiao, Y., B. Ma, D. McElheny, S. Parthasarathy, F. Long, M. Hoshi, R. Nussinov, and Y. Ishii. 2015. Abeta(1-42) fibril structure illuminates self-recognition and replication of amyloid in Alzheimer's disease. Nat. Struct. Mol. Biol. 22:499-505.
- 79. Vold, R. L., and R. R. Vold. 1991. Deuterium Relaxation in Molecular Solids. In Advances in Magnetic and Optical Resonance. W. Warren, Ed. Acadenic Press, San Diego. 85-171.
- 80. Vugmeyster, L., and D. Ostrovsky. 2019. Deuterium Rotating Frame NMR Relaxation Measurements in the Solid State under Static Conditions for Quantification of Dynamics. Chemphyschem 20:333-342.
- 81. Larsen, F. H., H. J. Jakobsen, P. D. Ellis, and N. C. Nielsen. 1998. High-field QCPMG-MAS NMR of half-integer quadrupolar nuclei with large quadrupole couplings. Mol. Phys. 95:1185-1195.
- 82. Petkova, A. T., R. D. Leapman, Z. H. Guo, W. M. Yau, M. P. Mattson, and R. Tycko. 2005. Self-propagating, molecular-level polymorphism in Alzheimer's beta-amyloid fibrils. Science. 307:262-265.
- 83. Noy, D., I. Solomonov, O. Sinkevich, T. Arad, K. Kjaer, and I. Sagi. 2008. Zinc-amyloid-beta interactions on a millisecond time-scale stabilize non-fibrillar Alzheimer-related species. J. Am. Chem. Soc. 130:1376-1383.

- 84. Vugmeyster, L., M. A. Clark, B. I. Falconer, D. Ostrovsky, D. Gantz, W. Qiang, and G. L. Hoatson. 2016. Flexibility and solvation of amyloid -beta hydrophobic core. J. Biol. Chem. 291:18484-18495.
- 85. Iadanza, M. G., M. P. Jackson, S. E. Radford, and N. A. Ranson. 2016. MpUL-multi: Software for Calculation of Amyloid Fibril Mass per Unit Length from TB-TEM Images. Sci. Rep. 6:21078.
- 86. Kurouski, D. 2016. Supramolecular Organization of Amyloid Fibrils. In Exploring New Findings on Amyloidosis. A.-M. Fernandez-Escamilla, editor. InTech, Rijeka. Ch. 02.
- 87. Palmer, A. G., 3rd. 2014. Chemical exchange in biomacromolecules: past, present, and future. J. Magn. Reson. 241:3-17.
- 88. Schanda, P., and M. Ernst. 2016. Studying Dynamics by Magic-Angle Spinning Solid-State NMR Spectroscopy: Principles and Applications to Biomolecules. Prog. Nucl. Magn. Reson. Spectrosc. 96:1-46.
- 89. Tollinger, M., A. C. Sivertsen, B. H. Meier, M. Ernst, and P. Schanda. 2012. Site-Resolved Measurement of Microsecond-to-Millisecond Conformational-Exchange Processes in Proteins by Solid-State NMR Spectroscopy. J. Am. Chem. Soc. 134:14800-14807.
- 90. Krushelnitsky, A., D. Gauto, D. C. Rodriguez Camargo, P. Schanda, and K. Saalwachter. 2018. Microsecond motions probed by near-rotary-resonance R1rho(15)N MAS NMR experiments: the model case of protein overall-rocking in crystals. J. Biomol. NMR. 71:53-67.
- 91. Li, K., P. S. Emani, J. Ash, M. Groves, and G. P. Drobny. 2014. A study of phenylalanine side-chain dynamics in surface-adsorbed peptides using solid-state deuterium NMR and rotamer library statistics. J. Am. Chem. Soc. 136:11402-11411.
- 92. Adler, J., H. A. Scheidt, M. Kruger, L. Thomas, and D. Huster. 2014. Local interactions influence the fibrillation kinetics, structure and dynamics of A beta(1-40) but leave the general fibril structure unchanged. Phys. Chem. Chem. Phys. 16:7461-7471.
- 93. Harris, J. R., and J. W. Horne. 1991. Negative Staining. In Electron Microscopy in Biology. J. R. Harris, editor. Oxford: IRL Press. 203-228.
- 94. Dubochet, J., M. Groom, and S. Mueller-Neuteboom. 1082. The mounting of macromolecules for electron microscopy with particular reference to surface phenomena and the treatment of support films by glow discharge. In Adv. Opt. Electron Microsc. R. Barrer, and V. E. Cosslett, Eds. 107-135.
- 95. Gor'kov, P. L., E. Y. Chekmenev, C. Li, M. Cotten, J. J. Buffy, N. J. Traaseth, G. Veglia, and W. W. Brey. 2007. Using low-E resonators to reduce RF heating in biological samples for static solid-state NMR up to 900 MHz. J. Magn. Reson. 185:77-93.
- 96. Persson, P.-O., and G. Strang. 2004. A Simple Mesh Generator in MATLAB. SIAM Rev. 46:329-345.
- 97. Namba, K., and G. Stubbs. 1986. Structure of tobacco mosaic virus at 3.6 A resolution: implications for assembly. Science. 231:1401-1406.
- 98. Parr, W. C., and W. R. Schucany. 1980. Minimum Distance and Robust Estimation. J. Am. Stat. Assoc. 75:616-624.
- 99. Vold, R. L., and G. L. Hoatson. 2009. Effects of jump dynamics on solid state nuclear magnetic resonance line shapes and spin relaxation times. J. Magn. Reson. 198:57-72.
- 100. Vega, A. J. (1992) MAS NMR spin locking of half-integer quadrupolar nuclei, J. Magn. Reson. 96, 50-68.
- 101. van der Maarel, J. R. C. The relaxation dynamics of spin 1=1 nuclei with a static quadrupolar coupling and a radio-frequency field, J Chem Phys 99, 5646-5653.
- 102. Abragam, A. (1961) Principles of Nuclear Magnetism, Clarendon Press, Oxford.